Journal of Materials Chemistry C

ROYAL SOCIETY OF CHEMISTRY

PAPER

View Article Online
View Journal | View Issue

Cite this: J. Mater. Chem. C, 2024, 12, 5578

Ferroelectricity of alkylamide-substituted triptycene derivatives†

Ryohei Mizoue,[a] Takashi Takeda,[abc] Shun Dekura,[ab] Mikiya Kato,[de] Tomoya Fukui,[de] Yoshiaki Shoji,[de] Takanori Fukushima,[def] Saya Yamane,[g] Yasutaka Suzuki,[g] Jun Kawamata[g] and Tomoyuki Akutagawa *[ab]

Received 24th December 2023,
Accepted 14th March 2024

DOI: 10.1039/d3tc04752k

rsc.li/materials-c

1,8,13-Tris(dodecyloxy)triptycene forms uniform two-dimensional (2D) thin films by self-assembly. We synthesized new 1,8,13- and 1,8-substituted triptycene derivatives in which the alkoxy chains were replaced with alkylamide chains capable of hydrogen-bonding and investigated their phase transition behaviors, molecular assembly structures, and dielectric properties. In the three-chain compounds, the formation of a tightly packed 2D structure dominated by one-dimensional (1D) intermolecular N–H···O= hydrogen bonds was observed. In the two-chain compounds, the molecular arrangement and hydrogen bonding patterns were different from those of the three-chain molecules due to the decrease in the occupied volume of the alkyl chains and molecular symmetry, and the disorder in the molecular arrangement increased in the hydrophobic moiety. Both compounds exhibit solid-to-solid and solid-to-liquid phase transitions without forming a liquid-crystalline phase. In the temperature- and frequency-dependent dielectric constants, thermally activated dynamics of the polar amide groups with increasing temperature was observed at low frequencies, accompanied by a hysteresis in the polarization–electric field (P–E) curve above 400 K, which is a characteristic of ferroelectrics.

Introduction

Since the structures and physical properties of molecular crystals are governed by intermolecular interactions on various energy scales, controlling the arrangement of the components by considering the manner of intermolecular interactions is essential in developing functions for molecular assemblies. For example, organic π-molecules tend to adopt one-dimensional (1D) π-stacked structures, resulting in electrically conducting crystals, and exhibit metal–insulator transitions, due to the instability of their 1D electronic systems and carrier trapping by impurities.[1–4] In order to suppress the phase transition to the insulator at low temperatures, the formation of a two-dimensional (2D) molecular arrangement has attracted attention from the viewpoint of stabilizing the metallic state, realizing superconducting and high carrier transport properties.[5–10] On the other hand, the 2D lamellar phases formed by amphiphilic organic molecules have been known to form Langmuir–Blodgett films.[11,12] In addition, a variety of functional 2D organic–inorganic hybrid perovskites have been developed by designing organic cations to achieve physical properties such as ferroelectricity, opto-electric responses, magnetism, and thermal conductivity.[13–16]

An interesting π-skeleton capable of forming 2D molecular arrays by self-assembly has been developed using triptycene.[17–19] For instance, 1,8,13-tris(dodecyloxy)triptycene, in which three dodecyl ether chains are introduced at the 1, 8, and 13-positions of triptycene, can form 2D thin films on a variety of substrate surfaces.[17] The 2D arrangement of the triptycene moieties with three-fold symmetry provides the molecular thin films with excellent stability and flexibility *via* the aid of multi-point van der Waals interactions between the alkyl chains. Applications of a 2D molecular layered structure to organic transistors and thermoplastic materials have already been reported.[20–25] Thus, 1,8,(13)-substituted triptycene represents an interesting molecular motif for the design of organic functional materials featuring 2D structural elements.

[a] Graduate School of Engineering, Tohoku University, Sendai 980-8579, Japan
[b] Institute of Multidisciplinary Research for Advanced Materials (IMRAM), Tohoku University, 2-1-1 Katahira, Aoba-ku, Sendai 980-8577, Japan. E-mail: akutagawa@tohoku.ac.jp
[c] Faculty of Science, Shinshu University, 3-1-1 Asahi, Matsumoto 390-8621, Japan
[d] Laboratory for Chemistry and Life Science, Institute of Innovative Research, Tokyo Institute of Technology, Yokohama 226-8503, Japan
[e] School of Materials and Chemical Technology, Tokyo Institute of Technology, Yokohama 226-8503, Japan
[f] Living Systems Materialogy (LiSM) Research Group, International Research Frontiers Initiative (IRFI), Tokyo Institute of Technology, 4259 Nagatsuta, Midori-ku, Yokohama 226-8503, Japan
[g] Graduate School of Sciences and Technology for Innovation, Yamaguchi University, 1677-1 Yoshida, Yamaguchi, 753-8512, Japan

† Electronic supplementary information (ESI) available. CCDC 2295387. For ESI and crystallographic data in CIF or other electronic format see DOI: https://doi.org/10.1039/d3tc04752k

The development of functional organic materials based on dynamic molecular assemblies has attracted much attention in recent years.[26–32] For example, proton and ion dynamics in molecular assemblies facilitate ferroelectricity and ionic conductivity,[33,34] and molecular rotational dynamics causes dielectric phase transitions and ferroelectricity.[35,36] Among the structural units that can be used to realize diverse dynamics in solids, alkylamide chains (–CONHC$_n$H$_{2n+1}$) are the most promising unit, because of their hydrophobic interactions and intermolecular N–H···O═ hydrogen bonding, both of which coexist in the molecular assemblies.[37–39] The formation of discotic hexagonal columnar (Col$_h$) liquid-crystalline phases has been reported for *N*,*N*′,*N*″-tri(tetradecyl)-1,3,5-benzenetricrboxamide with three alkylamide chains at the 1, 3, and 5-positions of benzene, and ferroelectricity with reversal of the polarization direction has been reported in the Col$_h$ phase when an external electric field is applied.[40–44] The inversion of polar intermolecular N–H···O═ hydrogen bonds along the 1D chains can result in a macroscopic dipole inversion, which is the origin of ferroelectricity. The partial melting of alkyl chains in the molecular assembly plays an important role in the inversion of intermolecular amide hydrogen bonds even in the solid state.[45] The π-electron cores at the molecular center have been utilized for pyrene,[46,47] tetrabenzoporphyrin,[48] and azobenzene,[49] in addition to benzene rings, and offer a lot of design freedom. 1D ferroelectrics can be formed by the formation of π-stacks and intermolecular N–H···O═ hydrogen bonds. The introduction of alkylamide chains into nonplanar π-electron compounds such as helicenes tends to form 2D hydrogen-bonding networks, increasing the values of the physical properties in ferroelectrics, remanent polarization (P_r), and coercive electric field (E_c), compared to materials featuring 1D hydrogen-bonding chains.[50] Furthermore, the chiral design of intermolecular amide hydrogen-bonding chains plays an important role in controlling the physical properties of ferroelectrics by utilizing the dynamics of the molecules.[51,52]

Triptycene is an interesting research target as a π-core to introduce multiple alkylamide chains. In previous studies, introduction of alkylamide chains into disc-shaped π-molecules such as benzene and pyrene resulted in the formation of 1D columnar structures and 1D ferroelectrics. The introduction of alkylamide chains into triptycene has the potential to form molecular assemblies that differ from 1D structures. Since triptycene easily adopts a 2D π-interdigitated layered structure and forms a stable 2D arrangement by self-assembly of alkyl chains through van der Waals interactions, the formation of intermolecular hydrogen bonding through additional amide units is expected to affect the 2D layered structure. In this study, we synthesized *N*,*N*′,*N*″-tritetradecyl-1,8,13-triptycenetricarboxamide (**C14TATP**) and *N*,*N*′-ditetradecyl-1,8-triptycenedicarboxamide (**C14DATP**) and investigated their phase transition behaviors, assembly structures, and dielectric properties and succeeded in revealing **C14TATP** shows a tightly packed 2D structure dominated by one-dimensional (1D) intermolecular N–H···O═ hydrogen bonds and ferroelectricity by the inversion of the amide group in the solid phase (Scheme 1). The reduction in the number of alkyl chains in **C14DATP** produced randomness in the packing structure, which affected the dielectric response and ferroelectricity.

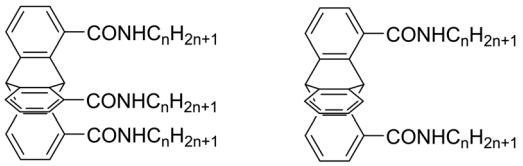

n = 6: **C6TATP** n = 14: **C14TATP** n = 6: **C6DATP** n = 14: **C14DATP**

Scheme 1 Molecular structures of **CnTATP** and **CnDATP** derivatives with n = 6 and 14 in this study.

Results and discussion

Phase transition behaviors

C14TATP and **C14DATP** were synthesized from 1,8,13-tricarboxytriptycene[53] and 1,8-dichlorotriptycene,[54] respectively (Experimental section in the ESI†). The thermal stabilities of **C14TATP** and **C14DATP** were expected to depend on the number of tetradecylamide chains that provide the strongest intermolecular interaction in the assemblies. TG measurements showed that **C14TATP** and **C14DATP** start to decompose at 600 and 500 K, respectively, and the thermal stability of the former is 100 K higher than that of the latter (Fig. S1, ESI†), due to the larger number of structural units that can contribute to intermolecular hydrogen bonding. Fig. 1a shows the DSC charts of **C14TATP** and **C14DATP**. Both compounds exhibit a reversible phase-transition behavior in multiple heating/cooling cycles. For **C14DATP**, a solid-to-solid phase transition from a lower temperature solid phase (S1) to another solid phase (S2) was observed at 292 K, and upon heating, S2 underwent a solid-to-isotropic liquid (IL) phase transition at 448 K. The transition enthalpy change (ΔH) for the S1–S2 phase transition was 22.7 kJ mol^{-1}, which was 65% smaller than that for the S2-IL phase transition (ΔH = 34.9 kJ mol^{-1}).

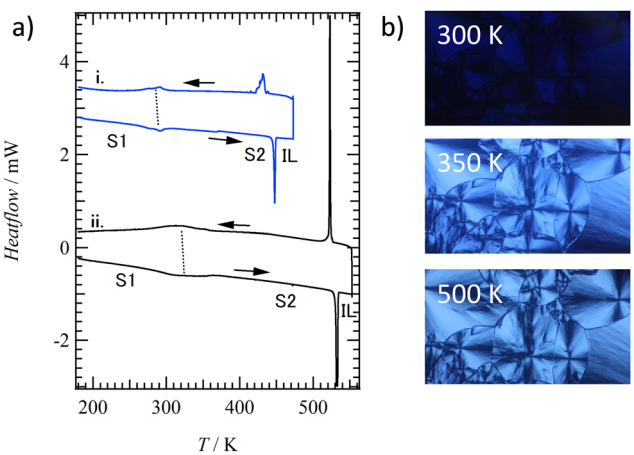

Fig. 1 Phase-transition behaviors. (a) DSC charts of **C14DATP** (blue i) and **C14TATP** (black ii) in the second heating cycle. (b) POM images of **C14TATP** at 300, 350, and 500 K.

A similar phase transition behavior was observed for the triple-chain compound, **C14TATP**, displaying S1–S2 and S2-IL phase transitions at 320 (ΔH = 30.9 kJ mol^{-1}) and 532 K (ΔH = 52.5 kJ mol^{-1}), respectively. Compared to **C14DATP**, the S2-IL phase transition temperature for **C14TATP** increased by 92 K, which was due to the presence of an additional intermolecular hydrogen bonding site that allows for the stabilization of the ordered phase up to higher temperatures. As expected, ΔH accompanying the S2-IL phase transition for **C14TATP** is 1.5 times larger than that for **C14DATP** (ΔH = 34.9 kJ mol^{-1}). Fig. 1b shows the change in the polarized optical microscopy (POM) image of **C14TATP** with increasing temperature. The S1 phase showed a dark field under a Cross-Nicol arrangement, whereas, upon the phase-transition into S2, the POM image turned bright with the emergence of a birefringent texture. This corresponds to a change in the domain orientation.

Crystal structure of C6TATP

Although, despite numerous trials, single crystals of **C14TATP** could not be obtained, those of **C6TATP**, suitable for X-ray crystallography, were successfully prepared by recrystallizing it from THF. However, the quality of the single crystals is not high enough to collect sufficient high-angle reflection data. Therefore, a detailed discussion of distances angles is not possible (Fig. S3, ESI†). Based on X-ray analysis, the crystal of **C6TATP** has a space group $P2_1/c$ at 100 K, and the asymmetric unit in the unit cell consists of one **C6TATP** molecule (Experimental section in the ESI† and Fig. S4).[55,56]

Fig. 2a and b show the assembly structures of **C6TATP** viewed along the *a*- and *c*-axis, respectively. **C6TATP** molecules form a layered structure with a 2D arrangement in the *bc* plane, where the neighboring molecules are aligned in such a way that the longer molecular axis orientations are opposite to each other. Unlike the 2D lamellar structure observed for 1,8,13-tris(dodecyloxy)triptycene, an interdigitated molecular assembly between the triptycene moieties was not observed. On the other hand, intermolecular N–H···O= hydrogen bonding interactions were observed along the *c*-axis, where the intramolecular and intermolecular N–O distances (d_{N-O}) were 2.847(2) Å, 2.802(8), and 2.749(7) Å, respectively. The intermolecular N–H···O= hydrogen bonds are stronger than intramolecular ones. Given that there are no effective intermolecular interactions along the *a*-axis that corresponds to the interlayer direction, the hydrogen-bonding interaction is considered to be the most effective intermolecular interaction in determining the packing structure of the molecular assembly.

Packing structures of C14TATP and C14DATP

To evaluate the molecular assembly structures of **C14TATP** and **C14DATP**, we carried out temperature-dependent PXRD experiments. Fig. 3a shows the temperature-dependent PXRD patterns of **C14TATP** and a simulated pattern obtained using the single crystal X-ray crystal data of **C6TATP** at 100 K. The diffraction peak of **C6TATP** at 2θ = 5.68° with a *d*-spacing of 15.56 Å arises from the stacking periodicity of the 2D layers, which corresponds to the *a*-axis length [15.8016(13) Å at 100 K]

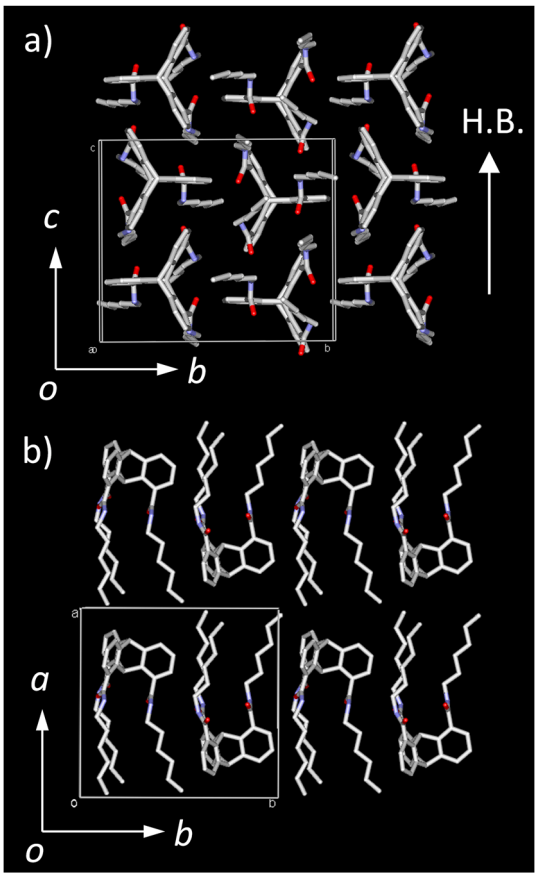

Fig. 2 Crystal structure of **C6TATP** at 100 K. Unit cell viewed (a) along the *a*-axis and (b) along the *c*-axis.

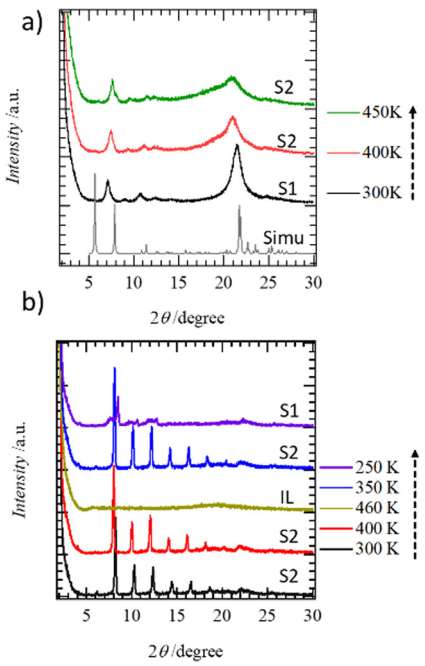

Fig. 3 Temperature-dependent PXRD patterns of (a) **C14TATP** and (b) **C14DATP**.

in the single crystal. For **C14TATP**, no significant differences in the PXRD patterns were observed between the S1 and S2 phases. At 300 K, diffraction patterns corresponding to a layer spacing of d = 25.5 Å appear at 2θ = 6.94 and 10.7°, which are assignable to 200 and 300 reflections of the a-axis for d_{200} = 12.73 and d_{300} = 8.261 Å. These are due to the stacking periodicity of the 2D layers. As the temperature was increased, the peak at 2θ = 21.7° with a d-spacing of 4.10 Å slightly shifts to become 2θ = 21.5° and 21.2° at 350 K and 400 K, respectively, and then broadens at 450 K. This broadening is the result of partial melting and thermal motion of the alkyl chains with increasing temperature.

Fig. 3b shows the temperature-dependent PXRD pattern of **C14DATP** with regular diffraction peaks appearing at 2θ = 4.09, 6.07, 8.11, 10.2, 12.2, 14.2. 16.3, and 18.4°. These can be well-explained by considering a layer periodicity with a d-spacing of 43.1 Å and correspond to correlation lengths of 1/2, 1/3, 1/4, 1/5, 1/6 1/8, and 1/9. Therefore, the molecular assembly of **C14DATP** has a 2D layered structure. We can now conclude that the dark-field POM images observed for the S1 and S2 phases are due to the formation of a homeotropic alignment perpendicular to the substrate surface, rather than randomly oriented domains. Notably, both **C14TATP** and **C14DATP** form 2D molecular assemblies with a layered lamellar structure, whereas the values of the layer periodicity (d = 25.5 and 43.1 Å for **C14TATP** and **C14DATP**, respectively) are very different from each other.

The molecular arrangements of **C14TATP** and **C14DATP** can be discussed in terms of 2D layered structures with different interlayer spacings. Assuming that the alkyl chains adopt an all-*trans* conformation, the maximum molecular lengths of **C14TATP** and **C14DATP** are estimated to be about 25 Å (Scheme 2a), with a thickness of about 7 Å for the triptycene moiety and an alkylamide chain length of about 18 Å. The molecular arrangement in **C14TATP** is expected to be dominated by 1D intermolecular N–H···O═ hydrogen bonds, as observed for single-crystalline **C6TATP**. The neighboring **C14TATP** molecules are arranged in upper and lower orientations with respect to each other, allowing the formation of a closest-packed structure even when the alkyl chain length is elongated from hexyl to tetradecyl chains (Scheme 2b). The amide N–H···O═ hydrogen bonds are formed in a direction parallel to the 2D layer. The molecular length of about 25 Å is in good agreement with an interlayer spacing of d = 25.5 Å found in the PXRD pattern.

C14DATP having two tetradecylamide chains gives a longer lamellar periodicity of d = 43.1 Å than **C14TATP**, suggesting that its closest-packing structure is different from that of **C14TATP**. The size of the triptycene moiety is compatible in volume with the three alkyl chains, and the formation of an interdigitated structure of the triptycene moiety and the closest-packing of the alkyl chains has been reported for a tris(alkoxyl)-substituted triptycene derivative that realizes a 2D sheet-like structure. In the case of double-chain compounds such as **C14DATP**, a space to be occupied by the alkyl chains remains in contrast with that in **C14TATP**, and the molecular arrangement is different from that of triple-chain compounds such as **C14TATP** to maintain the closest-packing structure. Considering the lamellar periodicity of d = 43.1 Å observed in the PXRD pattern of **C14DATP** as well as the formation of intermolecular N–H···O═ hydrogen bonds, a possible molecular arrangement can be proposed (Scheme 3). The lamellar periodicity (d = 43.1 Å) cannot be explained without assuming a dimer unit as a basic structure. It is reasonable to consider a dimer unit, in which the triptycene moieties interact in a face-to-face manner (left in Scheme 3a). The bilayer lamellar structure (d = 43.1 Å) can be explained if the alkyl chains are tilted about 54° with respect to the layer plane (Scheme 3b). Even in this case, intermolecular N–H···O═ hydrogen bonds are possibly formed in the in-plane direction of the bilayer structure. However, when the packing density of the alkyl chains is reduced, it appears difficult to form a closest-packing structure as in the case of three alkyl chains with an all-*trans* conformation. Therefore, the conformational and packing patterns of the alkyl chains in the **C14DATP** assembly are expected to be different to the case of **C14TATP**.

Temperature-dependent IR spectra

To evaluate the intermolecular N–H···O═ hydrogen bonding interactions in the **C14TATP** and **C14DATP** assemblies, temperature-dependent IR spectra of KBr pellets were measured (Fig. 4). **C14TATP** and **C14DATP** exhibit S1–S2 phase transitions at 318 and 291 K, respectively. At 300 K, the asymmetrical stretching vibrational bands (ν_{NH}) of the amide unit of **C14TATP** appear at two different energies of 3258 and 3318 cm^{-1}. The former ν_{NH} band is assigned to the

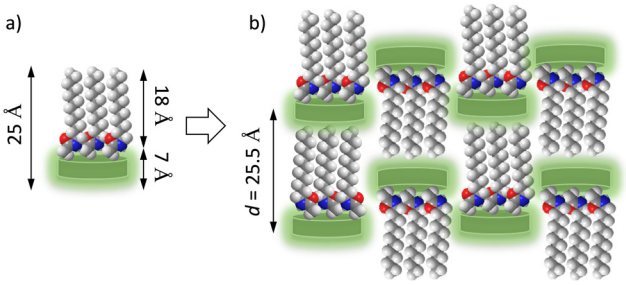

Scheme 2 Possible packing structure of **C14TATP**. (a) Schematic molecule and (b) its assembly strucuture.

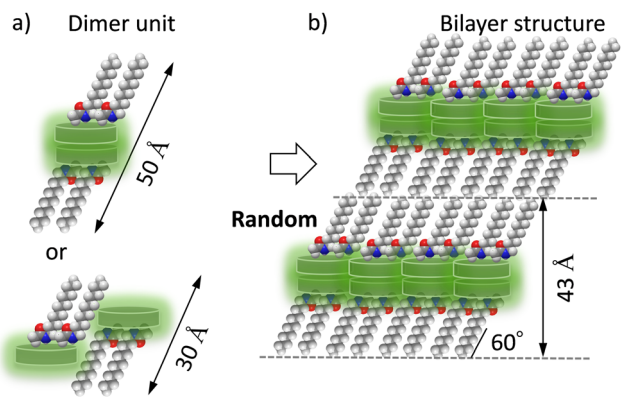

Scheme 3 Possible packing structure of **C14DATP**. (a) Schematic dimer molecular units and (b) its assembly strucuture.

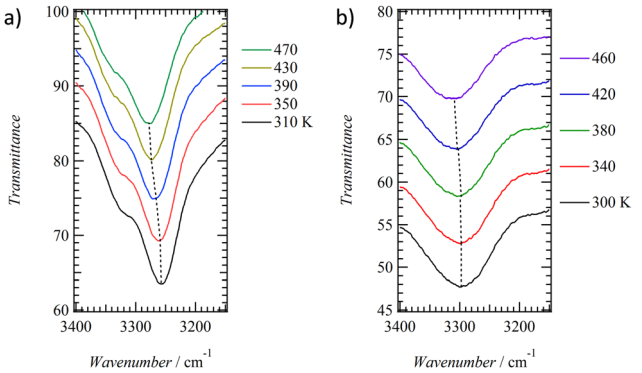

Fig. 4 Temperature-dependent IR spectra (KBr) of (a) **C14TATP** and (b) **C14DATP**.

intermolecular hydrogen-bonding amide groups, while the latter ν_{NH} band is assigned to the intramolecular hydrogen-bonding amide groups. The presence of amide groups in two different environments is consistent with the crystal structure of **C6TATP**. On the other hand, a broad ν_{NH} band is observed at 3299 cm^{-1} for the double-chain compound **C14DATP** at 300 K. The absence of ν_{NH} bands that are not involved in hydrogen bonding indicates that all the alkylamide chains in **C14DATP** contribute to intramolecular and intermolecular hydrogen-bonding interactions. The hydrogen-bonding ν_{NH} band for **C14DATP** is observed at higher energies than those for **C14TATP**, suggesting that a weaker hydrogen-bonding interaction is present in the former assembly.

Upon increasing the temperature from the S1 phase at room temperature to the S2 phase, the energy of the ν_{NH} band in each compound shows a blue-shift. For **C14TATP**, the ν_{NH} band at 470 K is observed at 3279 cm^{-1}, which is blue-shifted by approximately 20 cm^{-1} from that observed at 300 K. In contrast, the ν_{NH} band for **C14DATP** at 460 K is observed at 3279 cm^{-1}, with a blue-shift of 12 cm^{-1} compared to that at 300 K. The changes in the FWHM of the ν_{NH} bands for **C14TATP** and **C14DATP** upon increasing the temperature from 300 to 470 K are +14 and 0 cm^{-1}, respectively. The broadening of the ν_{NH} band for **C14TATP** is most likely due to an effect of randomness arising from thermal motion and disordering of hydrogen-bonding interactions. Therefore, the temperature increase results in thermal fluctuations in the N–H···O= hydrogen-bonding sites of **C14TATP**, leading to a change so that they can respond to external electric fields. On the other hand, given the fact that the ν_{NH} band of **C14DATP** remains almost intact with the temperature change and remains broad over a wide range including room temperature, and the N–H···O= hydrogen bonds with different strengths coexist in the assembly (Fig. S9, ESI†). We presume that in **C14DATP** having only two alkyl amide chains, a closest-packing of alkyl chains prevails over the formation of a structure with optimal hydrogen bonding between the amide groups, leading to randomness within the 2D structure and in turn the insensitivity of the ν_{NH} band to the temperature change.

Dielectric properties

Dielectric constants in molecular assemblies can vary in response to changes in the dipole moment of component molecules. The application of external electric fields to the **C14TATP** and **C14DATP** assemblies and/or temperature changes are expected to vary the orientation of amide groups involved in polar amide hydrogen bonds, resulting in a change in dielectric constants. Thus, we measured the temperature- and frequency-dependent real part dielectric constants (ε_1) of **C14TATP** and **C14DATP**. According to the DSC charts (Fig. 1a), both compounds exhibit the S1–S2 phase transition near room temperature. As shown in Fig. 5a, **C14TATP** displays no dielectric anomaly at around the S1–S2 phase transition at 300 K. Consistent with the fact that **C14TATP** has no intermediate phase such as the liquid crystal and plastic crystal, its temperature-dependent dielectric response was monotonous, and the dielectric response associated with changes in the dipole moment of the amide group was only observed in the higher temperature region. A periodic N–H···O= hydrogen bonding and a closest-packed structure in the 2D plane of the three alkyl-chains in **C14TATP** induced a rigid crystal lattice and dielectric response only at high temperatures.

The temperature- and frequency-dependent dielectric constants ε_1 of **C14DATP** (Fig. 5b) are different from those of **C14TATP**. A frequency-dependent broad peak varying from ε_1 ~3 to 3.5 was observed around 290 K, where the S1–S2 phase transition of **C14DATP** occurs. Upon further heating, the ε_1 value at a low frequency of 100 Hz increased from ~350 K. Compared to **C14TATP**, the observed frequency- and temperature-dependence of **C14DATP** is more pronounced,

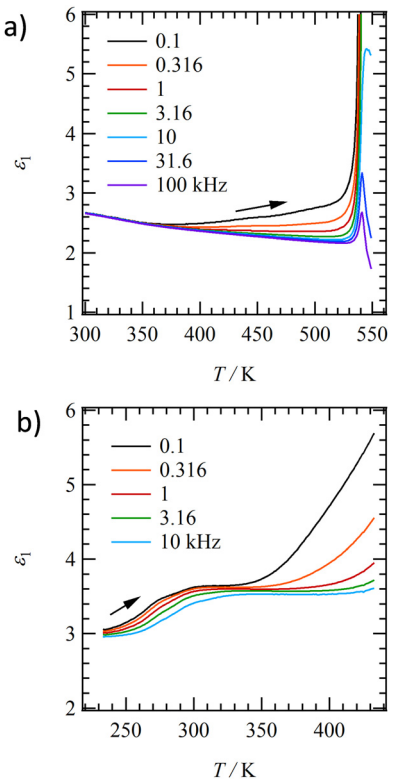

Fig. 5 Temperature- and frequency-dependent ε_1 of (a) **C14TATP** and (b) **C14DATP**.

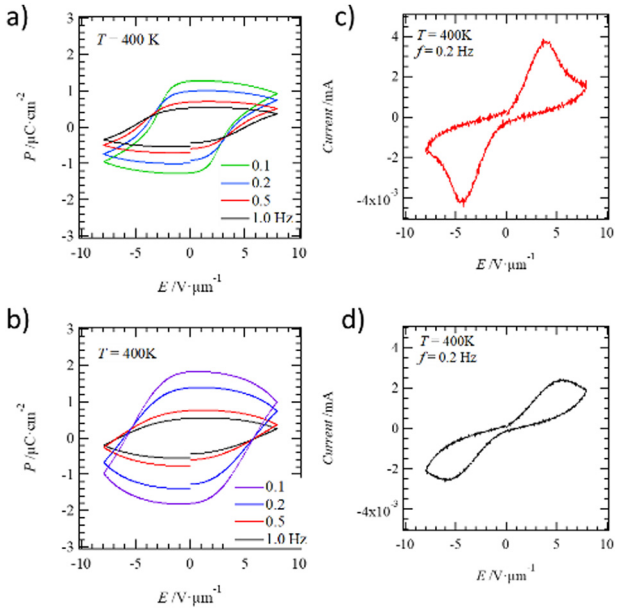

Fig. 6 Frequency-dependent *P*–*E* hysteresis curves of (a) **C14TATP** and (b) **C14DATP**. *I*–*E* plots of (c) **C14TATP** and (d) **C14DATP** at T = 400 K and f = 0.2 Hz.

and it can be concluded that the change in the dipole moment of **C14DATP** is greatly affected by the external field in the assembly. The imaginary part of the dielectric constant (ε_2) shows a frequency-dependent broad peak near the S1–S2 phase transition point, which is the characteristic of a single-Debye type relaxation process for the dielectric response. The random 2D arrangement of two alkylamide chains in **C14DATP** reduced the crystallinity and uniformity of the intermolecular N–H···O═ hydrogen-bonding network. The loose packing structure of **C14DATP** induced broad T- and f-dependent dipole responses. These results are consistent with the fact that the ν_{NH} band broadens around room temperature in the IR spectra of **C14DATP**.

P–*E* hysteresis curves

Fig. 6 shows the frequency-dependent polarization-electric field (*P*–*E*) curves and current-electric field (*I*–*E*) plots of **C14TATP** and **C14DATP** at 400 K. For both compounds, ferroelectric behavior with a *P*–*E* hysteresis was observed in the temperature range above 400 K, where the frequency-dependence is observed in the dielectric measurements. The effect of the leakage current on the *P*–*E* hysteresis of **C14DATP** near the melting point at 448 K becomes larger than that of **C14TATP**. The current (*I*)–*E* plots at 400 K show the *I*-maximum values corresponding to the polarization inversion of ferroelectricity. In addition, the symmetry in the ferroelectric phase is confirmed by SHG microscopy (Fig. S13, ESI†). The SHG activity of **C14TATP** is about 20% of that of granulated sugar at 298 K, supporting symmetry breaking. The fact that the sample shows SHG activity even when heated to 400 K is consistent with its ferroelectricity. In addition, SHG activity in the S2 phase is finely spread throughout the image. This corresponds to asymmetric, fine domains spread throughout in the molecule assembly structures. Similar *P*–*E* hysteresis curves have been observed in multiple alkylamide-substituted benzene derivatives that exhibit a Col_h liquid-crystal phase.[36–40]

In **C14TATP** and **C14DATP**, ferroelectricity was also observed in the *P*–*E* curves in the 2D structure in the solid state. The inversion motion of the hydrogen-bonded alkylamide chains within the 2D structure due to the electric field resulted in the polarization inversion and ferroelectricity. The thermally induced partial melting of the alkyl chains plays an important role in the reversal motion of the polar amide groups in hydrogen-bonding states. The remanent polarization (P_r) and coercive electric field (E_c) of **C14TATP** at 400 K with f = 0.2 Hz were 0.99 μC cm^{-2} and 3.88 V μm^{-1}, respectively, while those of **C14DATP** at 400 K with f = 0.2 Hz were 1.38 μC cm^{-2} and 5.82 V μm^{-1}. The P_r value of **C14DATP** is slightly larger than that of **C14TATP**; however, the magnitude of P_r for both compounds are same to each other accompanying a difference of leakage current. The similarity in P_r between **C14TATP** and **C14DATP** can be accounted for a scenario that only two of the three alkylamide chains in the former are involved in hydrogen-bonding interactions, and thus their contribution to the magnitude of P_r is the same as in **C14DATP**. On the other hand, the E_c value of **C14TATP** was smaller than that of **C14DATP**. This is because the formation of regular intermolecular N–H···O═ hydrogen bonds provides a constant barrier height for the dipole inversion. In the contrary, the disordered N–H···O═ hydrogen-bonds in the 2D structure of **C14DATP** generates a random energy barrier for the dipole inversion, which is thought to be the result of the increase in E_c.

Conclusions

1,8,13-Tris(dodecyloxy)triptycene having three alkyl chains at the 1, 8, and 13-positions of triptycene is known to form a particular 2D structure due to a combination of the nested packing of the triptycene moiety and van der Waals interactions of the three alkyl chains. Inspired by this finding, we prepared hydrogen-bonding triptycene derivatives by introducing alkyl amide –CONHC$_{14}$H$_{29}$ chains instead of the –OC$_{12}$H$_{25}$ chains. The phase transition behavior, molecular assembly structure, dielectric response, and ferroelectricity of **C14TATP** with three –CONHC$_{14}$H$_{29}$ chains, as well as those of **C14DATP** with two –CONHC$_{14}$H$_{29}$ chains, were investigated to evaluate the effect of the number of alkylamide chains on the molecular assembly structure and physical properties. 1D N–H···O═ hydrogen bonded chains were observed in both compounds, and ferroelectricity due to the inversion dynamics of the polar amide units was observed in the higher-temperature solid S2 phase above 400 K. Different dielectric responses between **C14TATP** and **C14DATP** were observed, and the dielectric response of the latter is dominated by the disordered packing of the alkylamide chains. The ν_{NH} band of **C14DATP** in the assembly was broadened compared to that of **C14TATP**, indicating the presence of disordered N–H···O═ hydrogen bonding interactions. The *P*–*E*

hysteresis was observed in the high-temperature S1 phase for both compounds, which is consistent with the presence of polarization inversion dynamics of the polar amide groups in the **C14DATP** assembly. The P_r values were comparable for both compounds, whereas the E_c values varied depending on the number of alkyl amide chains present. The intermolecular N–H···O= hydrogen bonds of **C14DATP** were more disordered than those of **C14TATP**, and the presence of structural randomness resulted in an increase in the polarization inversion energy. The design of alkylamide chains allows for the development of diverse ferroelectric molecular assemblies, and further design of π-electronic systems could lead to the creation of diverse multifunctional molecular materials.

Conflicts of interest

There are no conflicts to declare.

Acknowledgements

This work was supported by the Grant-in-Aid for Scientific Research on KAKENHI (Grant numbers: JP20H05865, JP22K19004, and JP20H05862 for T. A., and JP21H05024, JP21H04690, and JP20H05868 for Ta. F.), the Japan Science and Technology Agency, Core Research for Evolutional Science and Technology (Grant number: JPMJCR18I4), and the ''Crossover Alliance to Create the Future with People, Intelligence and Material'' project supported by the Ministry of Education, Culture, Sports, Science, and Technology.

Notes and references

1 L. B. Coleman, M. J. Cohen, D. J. Sandman, F. G. Yamagishi, A. F. Garito and A. J. Heeger, Superconducting Fluctuations and the Peierls Instability in an Organic Solid, *Solid State Commun.*, 1973, **12**, 1125–1132.

2 J. C. Scott, *Semiconductor and Semimetals: High Conducting Quasi-One-Dimensional Organic Crystals*, Academic Press, San Diego, 1988.

3 H. T. Nicolai, M. Kuik, G. A. H. Wetzelaer, B. Boer, C. Campbell, C. Risko, J. L. Brédas and P. W. M. Blom, Unification of Trap-Limited Electron Transport in Semiconducting Polymers, *Nat. Mater.*, 2012, **11**, 882–887.

4 O. Sachnik, X. Tan, D. Dou, C. Haese, N. Kinaret, K. H. Lin, D. Andrienko, M. Baumgarten, R. Graf, G. J. A. H. Wetzelaer, J. J. Michels and P. W. H. Blom, Elimination of Charge-Carrier Trapping by Molecular Design, *Nat. Mater.*, 2023, **22**, 1114–1120.

5 D. Jérome and H. J. Schulz, Organic Conductors and Superconductors, *Adv. Phys.*, 1982, **31**, 299–490.

6 G. Saito and Y. Yoshida, Development of Conductive Organic Molecular Assemblies: Organic Metals, Superconductors, and Exotic Functional Materials, *Bull. Chem. Soc. Jpn.*, 2007, **80**, 1–137.

7 H. Ebata, T. Izawa, E. Miyazaki, K. Takimiya, M. Ikeda, H. Kuwabara and T. Yui, Highly Soluble [1]Benzothieno[3,2-*b*]benzothiophene (BTBT) Derivatives for High-Performance, Solution-Processed Organic Field-Effect Transistors, *J. Am. Chem. Soc.*, 2007, **129**, 15732–15733.

8 H. Minemawari, M. Tanaka, S. Tsuzuki, S. Inoue, T. Yamada, R. Kumai, Y. Shimoi and T. Hasegawa, Enhanced Layered-Herringbone Packing Due to Long Alkyl Chain Substitution in Solution-Processable Organic Semiconductors, *Chem. Mater.*, 2017, **29**, 1245–1254.

9 Z. F. Yao, J. Y. Wang and J. Pei, Control of π–π Stacking via Crystal Engineering in Organic Conjugated Small Molecule Crystals, *Cryst. Grow. Des.*, 2018, **18**, 7–15.

10 H. Abe, A. Kawasaki, T. Takeda, N. Hoshino, W. Matsuda, S. Seki and T. Akutagawa, Crystal Lattice Design of H_2O-Tolerant n-Type Semiconducting Dianionic Naphthalenediimide Derivatives, *J. Am. Chem. Soc.*, 2021, **143**, 1046–1060.

11 B. K. Blodgett, Films Built by Depositing Successive Monomolecular Layers on a Solid Surface, *J. Am. Chem. Soc.*, 1935, **57**, 1007.

12 O. N. Oliveira, L. Caseli and K. Ariga, The Past and the Future of Langmuir and Langmuir–Blodgett Films, *Chem. Rev.*, 2022, **122**, 6459–6513.

13 W. Q. Liao, Y. Zhang, C. L. Hu, J. G. Mao, H. Y. Ye, P. F. Li, S. D. Huang and R. G. Xiong, A Lead-Halide Perovskite Molecular Ferroelectric Semiconductor, *Nat. Commun.*, 2015, **6**, 7338.

14 Z. Sun, X. Liu, T. Khan, C. Ji, A. M. Asghar, S. Zhao, L. Li, M. Hong and J. Luo, A Photoferroelectric Perovskite-Type Organometallic Halide with Exceptional Anisotropy of Bulk Photovoltaic Effects, *Angew. Chem., Int. Ed.*, 2016, **55**, 6545–6550.

15 K. Taniguchi, M. Nishio, N. Abe, P. J. Huang, S. Kimura, T. Arima and H. Miyasaka, Magneto-Electric Directional Anisotropy in Polar Soft Ferromagnets of Two-Dimensional Organic–Inorganic Hybrid Perovskites, *Angew. Chem., Int. Ed.*, 2021, **60**, 14350–14354.

16 N. Hoshino, S. Tamura and T. Akutagawa, Negative-to-Positive Thermal Conductivity Temperature Coefficient Transition Induced by Dynamic Fluctuations of the Alkyl Chains in the Layered Complex $(C_4H_9NH_3)_2CuCl_4$, *Chem. – Eur. J.*, 2020, **26**, 2610–2618.

17 N. Seiki, Y. Shoji, T. Kajitani, F. Ishiwari, A. Kosaka, T. Hikima, M. Takata, T. Someya and T. Fukushima, Rational Synthesis of Organic Thin Films with Exceptional Long-Range Structural Integrity, *Science*, 2015, **348**, 1122–1126.

18 F. K. C. Leung, F. Ishiwari, T. Kajitani, Y. Shoji, T. Hikima, M. Takata, A. Saeki, S. Seki, Y. M. A. Yamada and T. Fukushima, Supramolecular Scaffold for Tailoring the Two-Dimensional Assembly of Functional Molecular Units into Organic Thin Films, *J. Am. Chem. Soc.*, 2016, **138**, 11727–11733.

19 F. Ishiwari, G. Nascimbeni, E. Sauter, H. Tago, Y. Shoji, S. Fujii, M. Kiguchi, T. Tada, M. Zharnikov, E. Zojer and T. Fukushima, Triptycene Tripods for the Formation of Highly Uniform and Densely Packed Self-Assembled Monolayers with Controlled Molecular Orientation, *J. Am. Chem. Soc.*, 2019, **141**, 5995–6005.

20 T. Yokota, T. Kajitani, R. Shidachi, T. Tokuhara, M. Kaltenbrunner, Y. Shoji, F. Ishiwari, T. Sekitani, T. Fukushima and T. Someya, A Few-Layer Molecular Film on Polymer Substrates to Enhance the Performance of Organic Devices, *Nat. Nanotechnol.*, 2018, **13**, 139–144.

21 M. Kondo, T. Kajitani, T. Uemura, Y. Noda, F. Ishiwari, Y. Shoji, T. Araki, S. Yoshimoto, T. Fukushima and T. Sekitani, Highly-Ordered Triptycene Modifier Layer Based on Blade Coating for Ultraflexible Organic Transistors, *Sci. Rep.*, 2019, **9**, 9200.

22 M. Kondo, T. Uemura, F. Ishiwari, T. Kajitani, Y. Shoji, M. Morita, N. Namba, Y. Inoue, Y. Noda, T. Araki, T. Fukushima and T. Sekitani, Ultralow-Noise Organic Transistors Based on Polymeric Gate Dielectrics with Self-Assembled Modifiers, *ACS Appl. Mater. Interfaces*, 2019, **11**, 41561–41569.

23 M. Sugiyama, S. Jancke, T. Uemura, M. Kondo, Y. Inoue, N. Namba, T. Araki, T. Fukushima and T. Sekitani, Mobility Enhancement of DNTT and BTBT Derivative Organic Thin-Film Transistors by Triptycene Molecule Modification, *Org. Electron.*, 2021, **96**, 106219.

24 F. Ishiwari, G. Okabe, H. Ogiwara, T. Kajitani, M. Tokita, M. Takata and T. Fukushima, Terminal Functionalization with a Triptycene Motif that Dramatically Changes the Structural and Physical Properties of an Amorphous Polymer, *J. Am. Chem. Soc.*, 2018, **140**, 13497–13502.

25 Y. Chen, F. Ishiwari, T. Fukui, T. Kajitani, H. Liu, X. Liang, K. Nakajima, M. Tokita and T. Fukushima, Overcoming the Entropy of Polymer Chains by Making a Plane with Terminal Groups: a Thermoplastic PDMS with a Long-Range 1D Structural Order, *Chem. Sci.*, 2023, **14**, 2431–2440.

26 T. Akutagawa, Chemical Design and Physical Properties of Dynamic Molecular Assemblies, *Bull. Chem. Soc. Jpn.*, 2021, **94**, 1400–1420.

27 T. Akutagawa, T. Takeda and N. Hoshino, Dynamics of Proton, Ion, Molecule, and Crystal Lattice in Functional Molecular Assemblies, *Chem. Commun.*, 2021, **57**, 8378–8401.

28 T. Akutagawa, H. Koshinaka, D. Sato, S. Takeda, S. Noro, H. Takahasi, R. Kumai, Y. Tokura and T. Nakamura, Ferroelectricity and Polarity Control in Solid State Flip-Flop Supramolecular Rotators, *Nat. Mater.*, 2009, **8**, 342–347.

29 T. Takeda, M. Ozawa and T. Akutagawa, Jumping Crystal of a Hydrogen-Bonded Organic Framework Induced by the Collective Molecular Motion of a Twisted π System, *Angew. Chem., Int. Ed.*, 2019, **58**, 10345–10352.

30 D. W. Fu, H. L. Cai, Y. Liu, Q. Ye, W. Zhang, Y. Zhang, X. Y. Chen, G. Giovannetti, M. Capone, J. Li and R. G. Xiong, Diisopropylammonium Bromide is a High-Temperature Molecular Ferroelectric Crystal, *Science*, 2013, **339**, 425–428.

31 S. Furukawa, J. Wu, M. Koyama, K. Hayashi, N. Hoshino, T. Takeda, Y. Suzuki, J. Kawamata, M. Saito and T. Akutagawa, Ferroelectric Columnar Assemblies from the Bowl-to-Bowl Inversion of Aromatic Cores, *Nat. Commun.*, 2021, **12**, 768.

32 H. Y. Liu, H. Y. Zhang, X. G. Chen and R. G. Xiong, Molecular Design Principles for Ferroelectrics: Ferroelectrochemistry, *J. Am. Chem. Soc.*, 2020, **142**, 15205–15218.

33 T. Akutagawa, S. Takeda, T. Hasegawa and T. Nakamura, Proton-Transfer and Dielectric Phase Transition in Molecular Conductor $(HDABCO^{+})_2(TCNQ)_3$, *J. Am. Chem. Soc.*, 2004, **126**, 291–294.

34 G. Yuan, Y. Kimura, T. Kobayashi, T. Takeda, N. Hoshino and T. Akutagawa, Ion Polarisation-Assisted Hydrogen-Bonded Ferroelectrics in Liquid Crystalline Domains, *Chem. Sci.*, 2021, **12**, 13520–13529.

35 X. Chen, X. Han and D. Q. Shen, PVDF-Based Ferroelectric Polymers in Modern Flexible Electronics, *Adv. Electron. Mater.*, 2017, **3**, 1600460.

36 J. Ichikawa, N. Hoshino, T. Takeda and T. Akutagawa, Collective In-plane Molecular Rotator Based on Dibromoiodomesitylene π-Stacks, *J. Am. Chem. Soc.*, 2015, **137**, 13155–13160.

37 Y. Matsunaga, M. Miyajima, Y. Nakayasu, S. Sakai and M. Yonenaga, Design of Novel Mesomorphic Compounds: *N*,*N*′,*N*′′-Trialkyl-1,3,5-benzenetricarboxamides, *Bull. Chem. Soc. Jpn.*, 1988, **61**, 207–210.

38 T. F. A. D. Greef, M. M. J. Smulders, M. Wolffs, A. P. H. J. Schenning, R. P. Sijbesma and E. W. Meijer, Supramolecular Polymerization, *Chem. Rev.*, 2009, **109**, 5687–5754.

39 T. Takeda and T. Akutagawa, Chemical Design of Organic Ferroelectrics Using Dynamics of Alkylamide Chains, *Chem. Commun.*, 2022, **58**, 11898–11912.

40 Y. Shishido, H. Anetai, T. Takeda, N. Hoshino, S. Noro, T. Nakamura and T. Akutagawa, Molecular Assembly and Ferroelectric Response of Benzenecarboxamides Bearing Multiple $-CONHC_{14}H_{29}$ Chains, *J. Phys. Chem. C*, 2014, **118**, 21204–21214.

41 C. F. C. Fitié, W. S. C. Roelofs, M. Kemerink and R. P. Sijbesma, Remnant Polarization in Thin Films from a Columnar Liquid Crystal, *J. Am. Chem. Soc.*, 2010, **132**, 6892–6893.

42 C. F. C. Fitié, W. S. C. Roelofs, P. C. M. M. Magusin, M. Wubbenhorst, M. Kemerink and R. P. Sijbesma, Polar Switching in Trialkylbenzene-1,3,5-tricarboxamides, *J. Phys. Chem. B*, 2012, **116**, 3928–3937.

43 I. Urbanaviciute, X. Meng, T. D. Cornelissen, A. V. Gorbunov, S. Bhattacharjee, R. P. Sijbesma and M. Kemerink, Tuning the Ferroelectric Properties of Trialkylbenzene-1,3,5-tricarboxamide (BTA), *Adv. Electron. Mater.*, 2017, **3**, 1600530.

44 I. Urbanaviciute, S. Bhattacharjee, M. Biler, J. A. M. Lugger, T. D. Cornelissen, P. Norman, M. Linares, R. P. Sijbesma and M. Kemerink, Suppressing Depolarization by Tail Substitution in an Organic Supramolecular Ferroelectric, *Phys. Chem. Chem. Phys.*, 2019, **21**, 2069–2079.

45 M. Kawana, R. Mizoue, T. Takeda, N. Hoshino and T. Akutagawa, Simple Molecular Ferroelectrics: N,N′-Dialkyl-terephthalamide Derivatives in the Solid Phase, *J. Mater. Chem. C*, 2022, **10**, 4208–4217.

46 H. Anetai, Y. Wada, T. Takeda, N. Hoshino, S. Yamamoto, M. Mitsuishi, T. Takenobu and T. Akutagawa, Fluorescent Ferroelectrics of Hydrogen-Bonded Pyrene Derivatives, *J. Phys. Chem. Lett.*, 2015, **6**, 1813–1818.

47 H. Anetai, K. Sambe, T. Takeda, N. Hoshino and T. Akutagawa, Nanoscale Effects in One-Dimensional Columnar Supramolecular Ferroelectrics, *Chem. Eur. J.*, 2019, **25**, 11233–11239.
48 J. Wu, T. Takeda, N. Hoshino, Y. Suzuki, J. Kawamata and T. Akutagawa, Ferroelectricity of a Tetraphenylporphyrin Derivative Bearing $-CONHC_{14}H_{29}$ Chains at 500 K, *J. Phys. Chem. C*, 2019, **123**, 22439–22446.
49 J. Wu, Q. Zhu, T. Takeda, N. Hoshino and T. Akutagawa, Ferroelectricity of Hydrogen-Bonded Azobenzene Derivatives, *ACS Appl. Electron. Mater.*, 2021, **3**, 3521–3529.
50 H. Anetai, T. Takeda, N. Hoshino, H. Kobayashi, N. Saito, M. Shigeno, M. Yamaguchi and T. Akutagawa, Ferroelectric Alkylamide-Substituted Helicene Derivative with Two-Dimensional Hydrogen-Bonding Lamellar Phase, *J. Am. Chem. Soc.*, 2019, **141**, 2391–2397.
51 J. Wu, T. Takeda, N. Hoshino and T. Akutagawa, Ferroelectric Low-Voltage ON/OFF Switching of Chiral Benzene-1,3,5-tricarboxamide Derivative, *J. Mater. Chem. C*, 2020, **8**, 10283–10289.
52 J. Wu, T. Takeda, N. Hoshino and T. Akutagawa, Ferroelectrics Coupled with Uni-Directional Rotation in Liquid Crystals, *J. Phys. Chem. C*, 2022, **126**, 3864–3871.
53 S. Das, G. Nascimbeni, R. O. Morena, F. Ishiwari, Y. Shoji, T. Fukushima, M. Buck, E. Zojer and M. Zharnikov, Porous Honeycomb Self-Assembled Monolayers: Tripodal Adsorption and Hidden Chirality of Carboxylate Anchored Triptycenes on Ag, *ACS Nano*, 2021, **15**, 11168–11179.
54 M. E. Tauchert, T. R. Kaiser, A. P. V. Gçthlich, F. Rominger, D. C. M. Warth and P. Hofmann, Phosphonite Ligand Design for Nickel-Catalyzed 2-Methyl-3-butenenitrile Isomerization and Styrene Hydrocyanation, *ChemCatChem*, 2010, **2**, 674–682.
55 Crystal structure: single crystal structure analysis software. Ver. 3.6, Rigaku corporation and molecular structure corporation, 2004.
56 G. M. Sheldrick, SHELX2014 Programs for Crystal Structure Analysis, Universitat Göttingen: Göttingen, Germany, 2014.

